C. R. Palevol 16 (2017) 690–701

Contents lists available at ScienceDirect

Comptes Rendus Palevol

www.sciencedirect.com

Human Palaeontology and Prehistory

Cortical bone mapping: An application to hand and foot bones in hominoids

Distribution topographique de l'os cortical : une application aux os de la main et du pied chez les hominoïdes

Zewdi J. Tsegai[a,1,*], Nicholas B. Stephens[a,1], Graham M. Treece[b], Matthew M. Skinner[a,c], Tracy L. Kivell[a,c], Andrew H. Gee[b]

[a] *Department of Human Evolution, Max Planck Institute for Evolutionary Anthropology, Leipzig, Germany*
[b] *Department of Engineering, University of Cambridge, Cambridge, UK*
[c] *Skeletal Biology Research Centre, School of Anthropology and Conservation, University of Kent, Canterbury, UK*

ARTICLE INFO

Article history:
Received 10 July 2016
Accepted after revision 7 November 2016
Available online 27 December 2016

Handled by Roberto Macchiarelli and Clément Zanolli

Keywords:
Cortex
Cortical thickness measurement
Behavioural reconstruction
Morphometric maps
Hominoid

Mots clés :
Cortex
Mesure de l'épaisseur corticale
Reconstruction comportementale
Cartes morphométriques
Hominoïde

ABSTRACT

Bone form reflects both the genetic profile and behavioural history of an individual. As cortical bone is able to remodel in response to mechanical stimuli, interspecific differences in cortical bone thickness may relate to loading during locomotion or manual behaviours during object manipulation. Here, we test the application of a novel method of cortical bone mapping to the third metacarpal (Mc3) and talus of *Pan*, *Pongo*, and *Homo*. This method of analysis allows measurement of cortical thickness throughout the bone, and as such is applicable to elements with complex morphology. In addition, it allows for registration of each specimen to a canonical surface, and identifies regions where cortical thickness differs significantly between groups. Cortical bone mapping has potential for application to palaeoanthropological studies; however, due to the complexity of correctly registering homologous regions across varied morphology, further methodological development would be advantageous.

RÉSUMÉ

La forme d'un os reflète simultanément le profil génétique et l'histoire comportementale d'un individu. L'os cortical est capable de remodelage en réponse à des stimuli mécaniques. Les différences interspécifiques dans l'épaisseur de l'os cortical peuvent donc être corrélées avec la charge mécanique exercée durant la locomotion ou la manipulation d'objets. Ici, nous présentons l'application d'une méthode novatrice pour cartographier la distribution de l'os cortical du troisième métacarpien et du talus chez *Pan*, *Pongo* et *Homo*. Cette méthode permet d'analyser l'épaisseur corticale sur toute la longueur de l'os et est applicable à tous les éléments osseux ayant une morphologie complexe. En outre, cette méthode permet de recaler chaque spécimen sur une surface canonique et d'identifier les régions où l'épaisseur

* Corresponding author.
E-mail address: zewdi_tsegai@eva.mpg.de (Z.J. Tsegai).
[1] Contributed equally to this work.

http://dx.doi.org/10.1016/j.crpv.2016.11.001
1631-0683/

corticale diffère significativement entre les groupes. Ce procédé peut être appliqué à des études paléoanthropologiques. Cependant, du fait de la complexité du recalage correct des régions homologues, des progrès méthodologiques futurs sont envisagés.

1. Introduction

Identifying skeletal variables that relate to functional patterns is essential for reconstructing the behaviour of extinct species. However, it is often unclear which morphological features are most functionally relevant, as some researchers focus on novel, derived features, with the intention of understanding evolutionary change, while others are interested in the entire morphological complex of features, aiming to reconstruct the way in which a species lived (Ward, 2002). This is a common problem in palaeoanthropology, and has led to differing interpretations of skeletal morphology in fossil hominins (e.g., Latimer, 1991; Stern, 2000; Ward, 2002). In this debate, more plastic morphological features that can adapt in response to an individual's behaviour are of critical importance.

As cortical bone is able to remodel during life in response to mechanical load – a concept known as bone functional adaptation – it has the potential to hold a signal of an individual's behaviour (see Ruff et al., 2006, and references therein). Bone adapts to loading in several ways, for example by increasing/decreasing mineralisation to adapt its stiffness, changing shape to alter load transmission, or increasing thickness (Currey, 2003, 2010). However, this is a complex process that is likely to vary depending on skeletal location and systemic factors such as age, hormones and genes (e.g., Lovejoy et al., 2003; Pearson and Lieberman, 2004). Moreover, individual factors such as the magnitude and frequency of strain and the previous loading history of the bone cells can also affect cortical remodelling (e.g., Frost, 1987; Pearson and Lieberman, 2004; Ruff et al., 2006). Experimental studies are not always able to demonstrate that bone structure is well adapted to withstand strains (Demes et al., 1998, 2001; Lieberman et al., 2004) or that bone morphology changes in the expected way (Wallace et al., 2015a). However, in general, studies have shown that cortical bone is able to respond to behaviour during an individual's lifetime (Carlson and Judex, 2007; Christen et al., 2014; Robling et al., 2002; Ruff et al., 2006), and thus analysis of cortical bone thickness holds potential for reconstructing behaviour in extinct species.

Within palaeoanthropology, numerous studies have investigated how cortical bone properties relate to behaviour in both extant and fossil taxa. These can be broadly separated into three methodologies:

- analysis of cross-sectional geometric properties either at midshaft or at several points throughout the length of the shaft (e.g., Carlson, 2005; Carlson et al., 2006, 2008; Davies and Stock, 2014; Marchi, 2005; Ruff, 2002, 2008; Ruff et al., 2013, 2015; Sarringhaus et al., 2005; Shaw and Stock, 2013);
- generating 2D colour maps of cortical thickness throughout the diaphysis, with potential for application to non-cylindrical, irregularly shaped elements, although as yet this has only been tested on tooth roots, and not the epiphyses of long bones (e.g., Bondioli et al., 2010; Jashashvili et al., 2015; Puymerail, 2013; Puymerail et al., 2012a, 2012b);
- analysis of bone profiles at the articular surfaces, some of which include both cortical bone and also the underlying trabecular structure (Carlson et al., 2013; Mazurier et al., 2010; Patel and Carlson, 2007).

These analyses have been conducted using both clinical and micro-computed tomography (microCT) (e.g., Lillie et al., 2015). Several studies have focused specifically on cortical bone of the hands (e.g., Lazenby, 1998; Marchi, 2005) and feet (e.g., Griffin and Richmond, 2005; Jashashvili et al., 2015; Marchi, 2005). Recent studies that have analysed cortical bone thickness identified subtle differences both between African apes and modern humans, and between modern and fossil *Homo* species (Jashashvili et al., 2015; Puymerail, 2013; Puymerail et al., 2012a, 2012b).

Here, we investigate the potential applications of a novel method of cortical thickness analysis, developed for medical research, which allows for statistical comparison between groups (Poole et al., 2011, 2012; Treece et al., 2010, 2012). The main advantage of this method is that, unlike previous methods, it allows measurement of cortical bone thickness throughout the entire bone, i.e., including the diaphysis, metaphysis and epiphyses, and as such is applicable to both long bones and to more complex elements. Moreover, in contrast to existing methods, which require registration to a 2D map (e.g., Bondioli et al., 2010), it enables generation of 3D colour maps for each taxon/group, as well as quantification and visualization of regions whose difference in cortical thickness between groups can be assessed for statistical significance.

We test the application of this method on comparative samples of hand (third metacarpal) and foot (talus) bones of extant hominoids and, in order to test the applicability of this method in specimens with taxonomic alteration, one early Holocene human (Arene Candide 2, third metacarpal). As the hands and feet are the direct contact between an individual and the substrate, they are likely to experience the initial forces of both locomotion and object manipulation. As such, the skeletal elements in these regions are likely to reflect loading from these behaviours. However, many bones of the hands and feet, particularly carpals and tarsals, have irregular and complex shapes. As such, existing methods of analysis may not be applicable because complex bones cannot be modelled as simple beams and

Table 1
Study sample.
Tableau 1
L'échantillon étudié.

Taxon	Mc3	Talus	Locomotor mode	Mean body mass (kg)[a]
Homo sapiens	21	9	Bipedal	54.4–62.2
Early Holocene *Homo sapiens* (Arene Candide 2)	1	–	Bipedal	–
Pan troglodytes verus	5	13	Knuckle-walking	41.3–59.7
Pongo sp.	5	–	Suspensory, torso-orthograde	35.6–78.5

[a] Sex specific mean body mass (F–M). Body masses from Smith and Jungers (1997).

their morphology cannot be easily mapped to a 2D plane for between-group comparisons.

In sum, we assess the utility of this method in an anthropological context for:

- comparing cortical thickness differences amongst taxa where there are also consistent differences in shape;
- comparing cortical thickness between taxa with systemic differences in cortical thickness between species;
- conducting statistical comparisons across small sample sizes, common in palaeoanthropology;
- applicability to taphonomically altered fossil specimens.

2. Methods

2.1. Sample and microCT scanning

This study tests application of a cortical bone thickness analysis to the third metacarpal (Mc3) and talus. The study sample for the Mc3 consists of *Homo sapiens* ($n = 21$), *Pan troglodytes verus* ($n = 5$), *Pongo* sp. ($n = 5$), and a subfossil *H. sapiens* individual, Arene Candide 2 ($n = 1$), from the early Holocene (9900–10,850 uncal BP) (Sparacello et al., 2015). For the talus, the sample includes two species: *H. sapiens* ($n = 9$) and *P. t. verus* ($n = 13$). Details of the study samples are shown in Table 1. All non-human apes were wild-caught individuals and the modern human sample is composed of nine individuals from Nubian Egypt (6th–11th century) (Paoli et al., 1993; Strouhal and Jungwirth, 1979), eight individuals from Tiera del Fuego (19th century) (Marangoni et al., 2011), and four individuals from Syracuse (20th century).

High-resolution microCT scans of the sample were collected using a SkyScan1173 scanner at 100–130 kV and 61–62 μA and a BIR ACTIS 225/300 scanner at 130 kV and 100–120 μA. Both CT scanners are housed at the Department of Human Evolution, Max Planck Institute for Evolutionary Anthropology (Leipzig, Germany). All scans were reconstructed as 2048 × 2048 16-bit tiff stacks. All specimens were analysed at an isotropic voxel size of around 33 microns (mean: 33 μm, range: 30–42 μm).

2.2. Cortical thickness measurement

Segmentation of the outer surface of the bone and measurement of cortical thickness were conducted using Stradwin v5.1a (http://mi.eng.cam.ac.uk/~rwp/stradwin) (following Treece et al., 2010, 2012). Contours were automatically segmented using a threshold-based segmentation at 20-30 slice intervals along the length of the bone, with minor manual correction of errors in contour definition (Fig. 1A and B). Interpolation of these contours enabled creation of an outer surface of the bone (Fig. 1C). Using this surface as a guide, around 10,000–15,000 independent measures of cortical bone thickness were made at each vertex, which were based on the grey value profile of the CT data (Fig. 1D). As the vertices were placed at similar geometric separations, the number of measurements was dependent on the size of the bone. These thickness values were mapped onto the surface to generate a colour map of cortical thickness for each individual, which could be smoothed in order to minimise the effect of erroneous measurements (Fig. 1E).

2.3. Specimen registration

For comparison of cortical bone thickness maps between specimens, an average (canonical) surface was created to which each individual surface was registered using wxRegSurf v13 (http://mi.eng.cam.ac.uk/~ahg/wxRegSurf/) (following Gee et al., 2015). To create the canonical surface, an initial specimen was chosen to which every surface in the sample was then registered to create an average of all individuals (Fig. 2A). For both the Mc3 and talus, the specimen chosen to begin creation of an average surface was an individual of *H. sapiens*. Each specimen was registered to the canonical surface in order to compare cortical thickness between specimens (Fig. 2B).

2.4. Protocol for processing fossil specimens

A common problem encountered with archaeological and fossil specimens is the presence of unwanted inclusions within the bone. In some of the samples included here, we found such inclusions were of a higher density than the bone, which may affect measurement of cortical thickness. The protocol for segmentation was therefore modified for these samples, with those steps taken during the processing of the Arene Candide 2 Mc3 being used as an illustration (Fig. 3). Non-bone inclusions were corrected by either removing the bright inclusions or reducing the brightness of the bone in these regions. Both were achieved by creating a label field within Avizo 8.1, where the magic wand tool was used to select the high-density

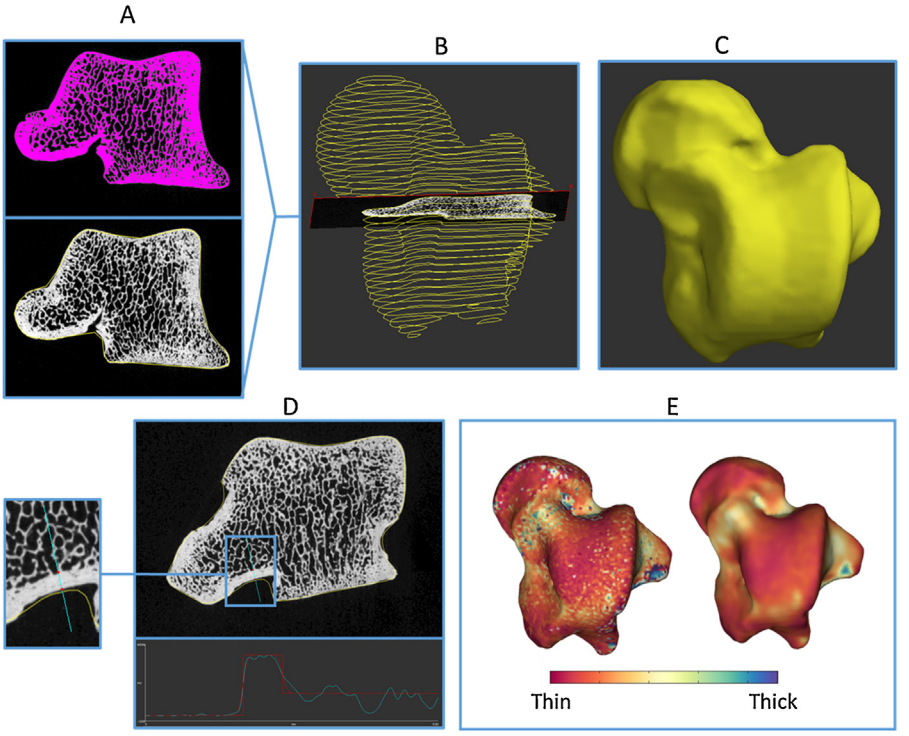

Fig. 1. Overview of the cortical thickness measurement protocol for a *Pan* talus. A. Segmentation of contours on an individual slice showing the threshold region in magenta (top) and subsequent yellow contour around bone (bottom). B. Contours are automatically drawn at 20–30 slice intervals throughout the bone. C. Contours are interpolated to generate a surface used as a guide for cortical thickness measurements. D. Measurement of cortical bone thickness along a line running through the cortex (top), measurement is based on the grey values shown in the interpolated data (graph, bottom). E. Cortical thickness maps are subsequently generated (left), which can be smoothed (right) to even out erroneous measurements. Thicker cortex is shown in blue and thinner cortex in red.

Fig. 1. Aperçu général du protocole de mesure de l'épaisseur corticale pour un talus de *Pan*. A. Segmentation des contours sur une coupe individuelle montrant la région seuillée en magenta (en haut) et le contour jaune subséquent autour de l'os (en bas). B. Les contours sont automatiquement tracés par intervalles de 20–30 coupes sur toute la longueur de l'os. C. Les contours sont interpolés pour générer une surface utilisée comme un guide pour les mesures d'épaisseur corticale. D. Mesure de l'épaisseur de l'os cortical le long d'une ligne parcourant l'épaisseur du cortex (en haut), la mesure est basée sur les valeurs de gris affichées dans les données interpolées (graphique, en bas). E. La distribution de l'épaisseur de l'os cortical est ensuite générée (à gauche) et peut être lissée (à droite) pour exclure de potentielles mesures aberrantes. L'os cortical le plus épais est figuré en bleu et le plus fin est en rouge.

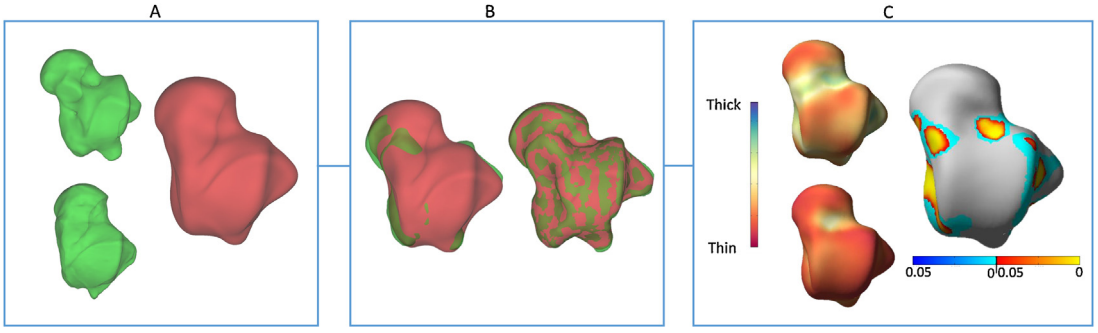

Fig. 2. Overview of registration to a canonical mesh and between-group comparisons of a *Pan* and *Homo* talus. A. Surface of one *Pan* (top left) and one *Homo* (bottom left) individual. Surface files from the complete sample were used to generate an average, canonical surface (right). B. An individual surface (green) and the canonical surface (red), before (left) and after (right) the registration. C. Mean cortical thickness maps of *Pan* (top left) and *Homo* (bottom left), both expressed on the canonical surface, and a map showing regions where there are significant differences between the two species (right). In the map of significant differences, regions in yellow-red show significant differences at each vertex and regions in blue (extending from yellow-red regions) show significant differences by cluster.

Fig. 2. Vue d'ensemble du recalage de talus de *Pan* et *Homo* sur un maillage canonique et comparaisons entre groupes. A. Surface d'un individu *Pan* (en haut à gauche) et d'un individu *Homo* (en bas à gauche). Les fichiers de surface de l'échantillon entier ont été utilisés pour générer une surface canonique moyenne (à droite). B. Surface individuelle (en vert) et surface canonique (en rouge), avant (à gauche) et après (à droite) le recalage. C. Distribution moyenne de l'épaisseur corticale chez *Pan* (en haut à gauche) et chez *Homo* (en bas à gauche), les deux étant projetées sur la surface canonique, et distribution montrant les régions où les deux espèces diffèrent significativement (à droite). Dans la carte montrant les différences significatives, les régions en couleurs chaudes montrent les différences significatives au niveau de chaque vertex, et les régions en couleurs froides (dépassant des régions en couleurs chaudes) indiquent les différences par *cluster*.

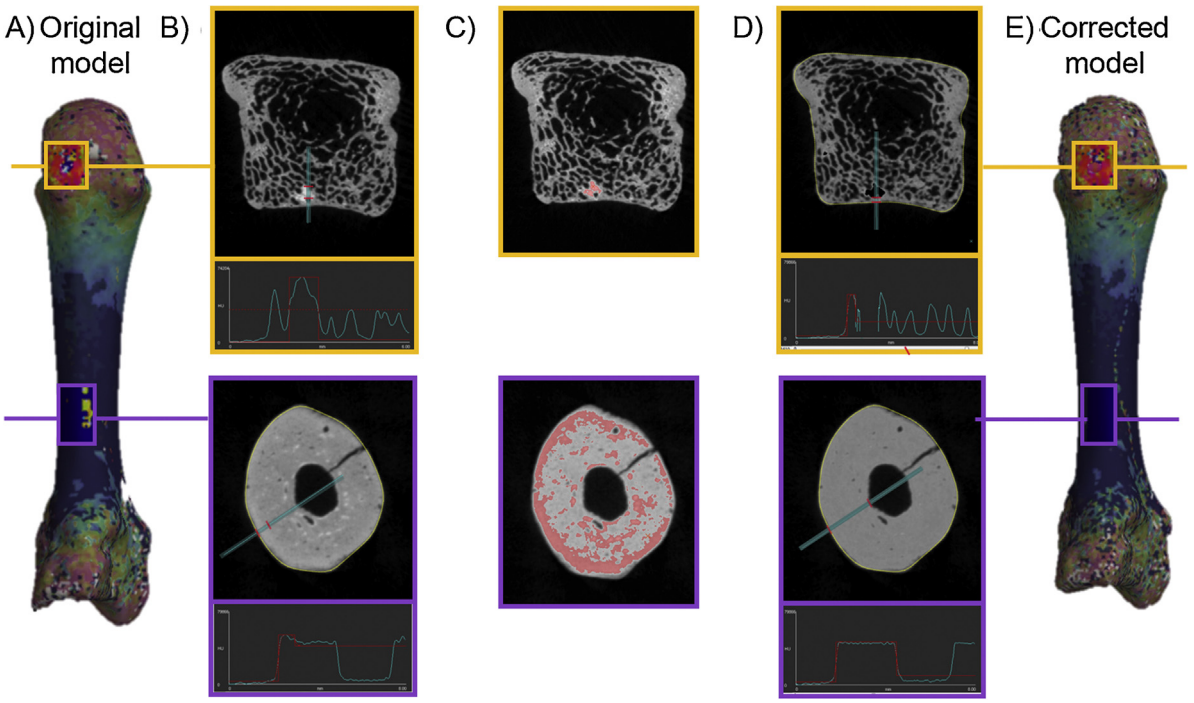

Fig. 3. Protocol for processing specimens with high-density inclusions. Shown here is the Mc3 of Arene Candide 2. Incorrect measurements on the original model (A) are due to high-density inclusions (B top) and differential preservation (B bottom) leading to artificially thick (orange box) and thin (purple box) regions of the colour map. High-density inclusions outside of the cortex are selected in the CT data, shown in magenta (C) and removed (D top), while high intensity grey values within the cortex are reduced with an arithmetic operation (D bottom) (see text for explanation), to create the corrected model (E).
Fig. 3. Protocole pour traiter les spécimens avec des inclusions à haute densité. Le troisième métacarpien d'Arene Candide 2 est ici illustré. Les mesures incorrectes sur le modèle original (A) sont dues à des inclusions à haute densité (B, en haut) et à une préservation différentielle (B, en bas) causant des régions artificiellement épaisses (encadré orange) et fines (encadré violet) sur la carte colorée. Les inclusions à haute densité en dehors du cortex sont sélectionnées (en rouge) dans les données CT (C) et enlevées (D, en haut), alors que les valeurs de gris correspondant aux hautes densités de l'os cortical sont réduites par une opération arithmétique (D, en bas) (voir le texte pour plus d'informations) pour créer le modèle corrigé (E).

materials. Those that were to be removed were subtracted from the original image with an arithmetic operation (i.e. original – label field), while those areas constrained along the exterior of the cortical bone were first multiplied by a fraction of their grey values and then subtracted from the original [i.e. original data – (label field × 0.05)]. This resulted in an even grey value range that would permit an accurate estimate of the cortical thickness for each measured point.

2.5. Statistical parametric mapping

Mean cortical thickness maps were generated for each taxon and between-group comparisons were conducted using statistical parametric mapping (Friston et al., 1995) in the SurfStat package (Worsley et al., 2009). In order to generate mean cortical thickness maps for each species, the species mean was calculated for each vertex of the registered surfaces. As the surfaces are registered to a canonical surface, these vertices are at equivalent locations. Statistical parametric maps, commonly used in neuroimaging, are in essence the mapped results of univariate comparisons at multiple points. In essence, this is a "mass-univariate" analysis in that univariate comparisons are made at each of the many vertices of the registered surface (Friston et al., 1995). We applied statistical parametric mapping to the registered surfaces in order to conduct interspecific comparisons. A general linear model (GLM) was fitted to the data to determine whether cortical thickness can be explained by covariates of interest (species/taxa) and confounding covariates. In order to minimise the effect of shape differences on systematic misregistration, we incorporated information about shape as a confounding covariate in the GLM (Gee and Treece, 2014; Gee et al., 2015). Specifically, we included non-rigid shape coefficients, which were generated from a statistical shape model via principal component analysis of the movement of each vertex during registration, as described in Gee and Treece (2014). The most dominant mode of shape variation, which largely captured bone size, was disregarded since this was highly correlated with taxa. Statistical parametric maps were generated using *F* statistics for pairwise comparisons (talus) or T statistics for multiple comparisons (Mc3), and the corresponding *P*-values were corrected for multiple comparisons using random field theory, in order to control for the chance of false positives (Fig. 2C) (Friston et al., 1995; Worsley et al., 2009). For statistical tests a *P*-value of $P < 0.05$ was considered significant. These statistical tests are conducted both for each vertex of the registered surface (Fig. 2C: yellow-red colour scale) and for localised regions, or clusters, on the registered surface (Fig. 2C: blue colour scale) (Friston et al., 1995). For the

Table 2
Mean cortical thickness values and standard deviations for the third metacarpal and talus.
Tableau 2
Valeurs moyennes et écarts-types de l'épaisseur corticale pour le troisième métacarpien et le talus.

	Mean cortical thickness (mm)	
Taxon	Mc3	Talus
Homo sapiens	1.03 (0.07)	0.45 (0.06)
Early Holocene *Homo sapiens* (Arene Candide 2)	1.40	–
Pan troglodytes verus	1.59 (0.19)	0.88 (0.19)
Pongo sp.	1.47 (0.10)	–

talus, relative thickness values were calculated for each individual by subtracting the individual mean value from all of the thickness measurements then dividing by the standard deviation, so as to test a method for standardising values when there are considerable interspecific differences in mean cortical thickness.

3. Results

Cortical thickness mean values and standard deviations are shown in Table 2. In the talus, *Pan* has thicker cortical bone than *Homo*. This is similar to the cortical bone in the Mc3, where both *Pongo* and *Pan* have thicker cortical bone than *Homo*. Within *Homo*, the Arene Candide 2 Mc3 has the thickest cortical bone, approaching the average of *Pongo*.

3.1. Cortical thickness maps: Mc3

Cortical thickness maps for the Mc3 are shown on Fig. 4. Both *Pan* and *Pongo* have much thicker cortical bone in the shaft compared with *Homo*, and in *Pongo* the regions of greater thickness extend further proximally and distally than in *Pan*. The non-human specimens also have greater cortical thickness than *Homo* at the epiphyses; however, no visible differences between the species can be discerned from the mean cortical thickness maps.

Quantitatively, the overall greater thickness of the Mc3 of Arene Candide 2, compared with modern humans, is in line with previous assessments of increased gracility of the skeleton in recent, more sedentary modern humans (Chirchir et al., 2015; Ryan and Shaw, 2015, but see Wallace et al., 2015b). Qualitatively, however, the local thickness pattern is largely comparable to that of recent *Homo*, where the thickest point of cortical bone is at the palmar aspect of the midshaft, while the cortex thins at the epiphyses. Interestingly, there is also thickening observable along the presumed attachment site of the second and third dorsal interosseous (Cashmore and Zakrzewski, 2013, but see Rabey et al., 2015; Williams-Hatala et al., 2016).

Fig. 5 shows the overall cortical thickness differences and statistically significant differences by region. A comparison between *Pongo* and *Homo* reveals that *Pongo* has thicker cortex along the majority of the diaphysis (Fig. 5, left), and this difference is statistically significant (Fig. 5, right), with further cortical differences at the palmar and dorso-ulnar aspect of the Mc3 head. Less dramatic differences exist between *Pan* and *Homo*, with *Pan* demonstrating significantly thicker cortical bone primarily along the dorsal aspect of the diaphysis and head, as well as a prominent region at the radial and ulnar aspects of the base that extends distally to the Mc2/Mc4 articular surfaces. *Pongo* and *Pan* differ in regions in which the cortical bone is both thicker and thinner; *Pongo* is relatively thinner than *Pan* along the dorsal aspect of the Mc3 diaphysis and head, but comparatively thicker along the palmar aspect of the diaphysis and dorsal aspect of the base. However, none of these differences in cortical thickness were statistically significant (Fig. 5).

3.2. Cortical thickness maps: talus

Cortical thickness maps for the talus are shown on Fig. 6A. The mean maps for each species, based on the absolute thickness values, show that *Homo* and *Pan* both share thicker cortical bone on the medial and lateral malleolar surfaces and on the medial aspect of the talar neck. *Pan*, but not *Homo*, has a region of thicker cortical bone on the posterior subtalar articular surface. However, the absolute thickness map (Fig. 6A) shows that overall *Homo* has thinner cortex throughout the talus compared with *Pan*. There are several regions of significant differences in cortical bone thickness between the species, which generally represent the regions in which *Pan* has the thickest cortical bone compared with *Homo*.

3.3. Relative means

To account for the significantly thicker cortex throughout the *Pan* talus, relative thickness maps were produced and are shown on Fig. 6B. Relative cortical thickness was calculated for each specimen by subtracting the individual mean value from each thickness measurement and dividing by the standard deviation. The regions in which the mean colour maps show relatively thicker cortical bone are similar to the absolute thickness maps. The comparison between the two species, however, shows a different pattern. There are regions in which *Pan* has relatively thicker cortical bone compared with *Homo*, particularly on the medial and lateral malleolar surfaces and on the medial aspect of the talar neck. In contrast, *Homo* has relatively thicker bone at the posterior talar tubercles, the posterior surface of the talar trochlea, and in some regions of the talar head. The regions in which cortical thickness differs significantly between the two species also differ between the absolute and relative colour maps.

4. Discussion

We sought to augment and expand upon well-established methods of cortical bone analysis for palaeoanthropological research by adapting an imaging technique originally designed for low resolution diagnostic medical CT scans. This 3D cortical mapping method (using freeware Stradwin v5.1a and wxRegSurf v13) is attractive because it allows for the rapid acquisition of thousands of independent measurements of cortical thickness using

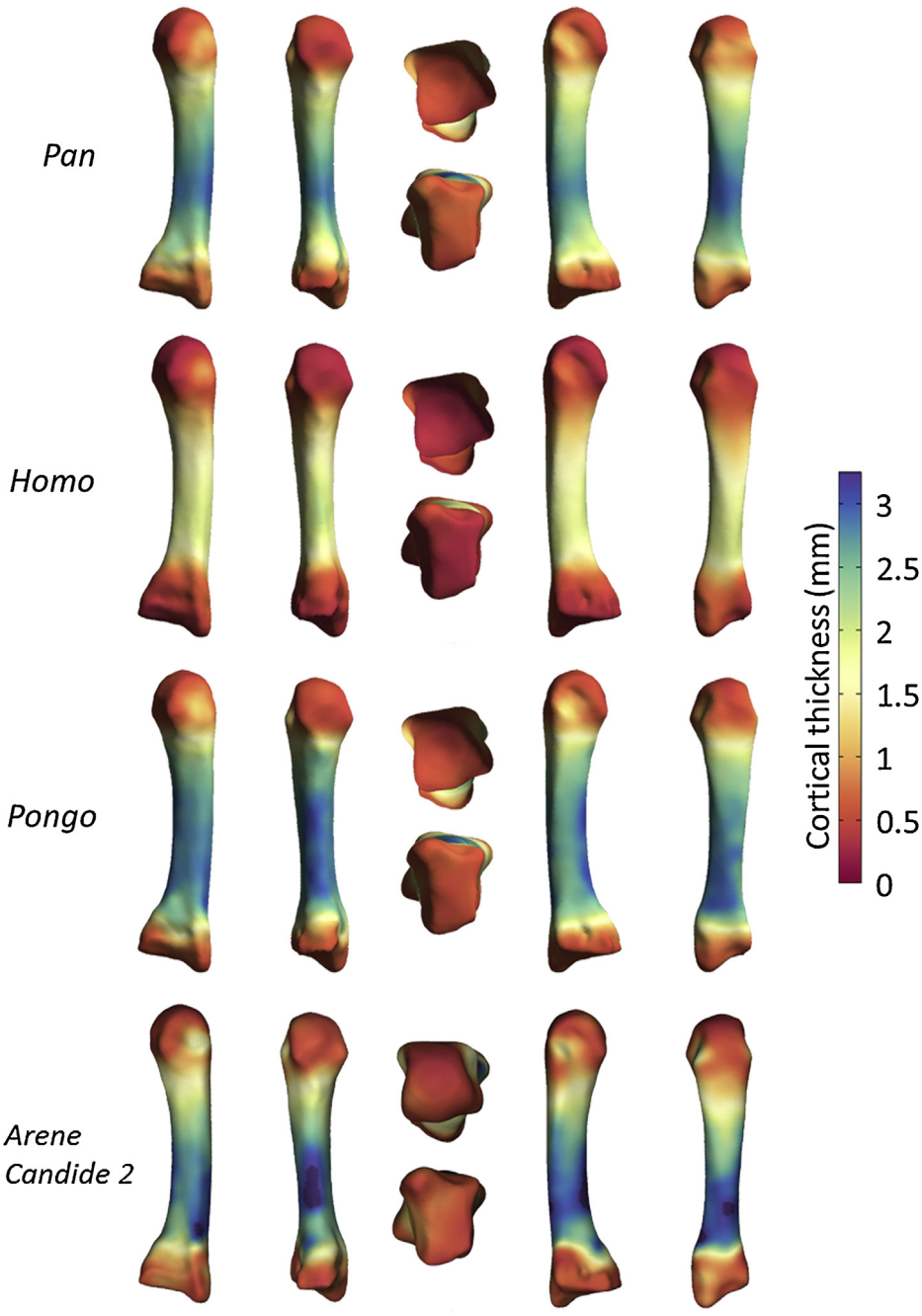

Fig. 4. Mean cortical thickness maps of the Mc3 for each species, all mapped to the canonical mesh. From top to bottom, *Pan*, *Homo*, *Pongo* and archaeological *Homo* (Arene Candide 2). Thicker cortex in is blue, thinner cortex in red. Metacarpals are shown in (left to right) lateral, palmar, distal (top), proximal (bottom), medial and dorsal views.

Fig. 4. Distributions moyennes de l'épaisseur de l'os cortical du troisième métacarpien pour chaque espèce, toutes recalées sur le maillage canonique. De haut en bas, *Pan*, *Homo*, *Pongo* et un spécimen *Homo* archéologique (Arene Candide 2). L'os cortical plus épais est figuré en bleu, celui plus fin est en rouge. Les métacarpiens sont montrés, de gauche à droite, en vues latérale, palmaire, distale (en haut), proximale (en bas), médiale et dorsale.

unsegmented CT data of relatively simple (e.g., femoral) and complex (e.g., vertebral) morphologies within a stand-alone and freely available software package. Such measurements may then be mapped onto a canonical bone of mean shape for qualitative and quantitative comparison (i.e., using statistical parametric mapping; Friston et al., 1995; Gee and Treece, 2014). Within the present study we found that this method is capable of analysing and visualizing cortical thickness data from high-resolution microCT scans of hominoid metacarpals and tali, which present two distinctly different morphologies.

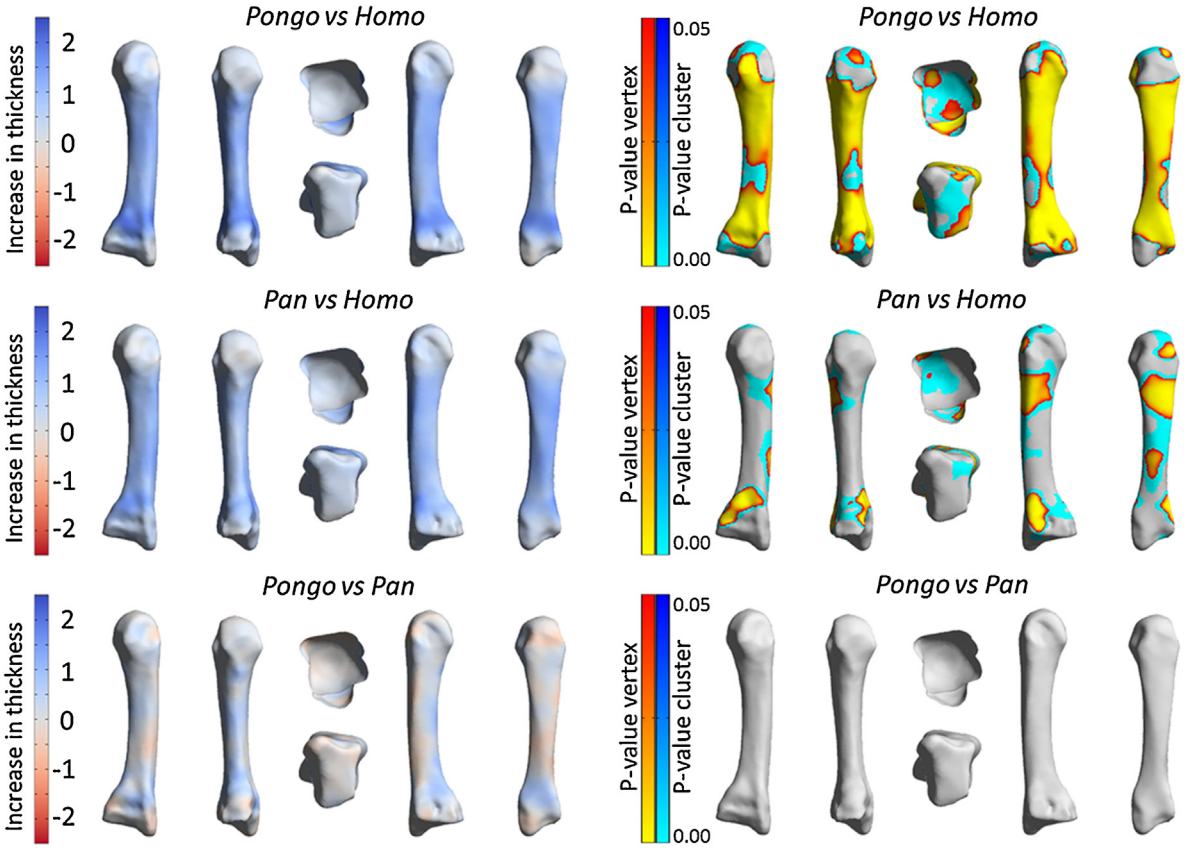

Fig. 5. Colour maps of cortical thickness differences between each species (left) and statistical comparisons (right) for the Mc3 in (top to bottom) *Pongo* vs. *Homo*, *Pan* vs. *Homo*, and *Pongo* vs. *Pan*. Differences in thickness between species (left) are blue where the first species has a thicker cortex than the second and red where the first species has a thinner cortex than the second. Statistical comparisons (right) show regions where there are significantly different cortical thickness values at each vertex (yellow-red), and regions where there are significant differences in cortical thickness at each cluster (blue). No significant differences were found between *Pan* and *Pongo*. Metacarpals are shown in (left to right) lateral, palmar, distal (top), proximal (bottom), medial and dorsal views.

Fig. 5. Cartes chromatiques des différences de distribution d'épaisseur de l'os cortical entre plusieurs paires d'espèces (à gauche) et comparaisons statistiques (à droite) pour le troisième métacarpien de *Pongo* et *Homo*, *Pan* et *Homo*, et *Pongo* et *Pan* (de haut en bas). Les différences d'épaisseur entre paires d'espèces (à gauche) sont figurées en bleu lorsque la première espèce montre un cortex plus épais que la seconde, et en rouge en cas d'épaisseur plus faible. Les comparaisons statistiques (à droite) montrent les régions pour lesquelles les différences d'épaisseur corticale sont significatives au niveau de chaque vertex (couleurs chaudes) et de chaque *cluster* (couleurs froides). Aucune différence significative n'a pu être identifiée entre *Pan* et *Pongo*. Les métacarpiens sont montrés, de gauche à droite, en vues latérale, palmaire, distale (en haut), proximale (en bas), médiale et dorsale.

Broadly speaking we found that the average cortical thickness of both the Mc3 and talus was relatively thinner in modern *Homo* when compared to *Pan*, *Pongo*, and the subfossil Mc3 of Arene Candide 2. Within the Mc3 of *Pan* and *Homo*, regions of greater thickness were concentrated in a band along the proximal-midshaft with the thinnest portion being found at the palmar surface of the proximal and distal articular surfaces. However, the greatest thickness in *Homo* is apparent along the palmar aspect of this band. *Pongo* differed from the other two groups in a noticeable absence of a thick band at midshaft, with thickening instead being found along the palmar aspect of the shaft and head. Although there were no statistically significant differences between *Pongo* and *Pan*, subtle variations in thickness are apparent along the dorsal aspect, where *Pongo* is relatively thinner at the head and dorsal aspect of the shaft but thicker at the base. It would be interesting to see if these differences reach significance with increased sample sizes. Within the talus, we found regions of greater thickness in both *Homo* and *Pan* on the medial and lateral malleolar surfaces and on the medial surface of the talar neck. In *Pan*, but not *Homo*, the posterior subtalar articular surface has very thick cortical bone. Statistically significant differences between *Pan* and *Homo* were then found and visualized using both raw and equalized data that supported the qualitative observations. Although not the goal of the present study, these results illustrate the potential of this method for identifying differences in cortical thickness between species that can be used to test hypotheses founded upon bone functional adaptation and known variation in behavioural loading.

Inherent to any method seeking to evaluate interspecific comparisons is the necessity of identifying homologous anatomical regions. The "whole bone" approach of this 3D cortical mapping method helps to overcome some challenges associated with identifying homologous subsamples

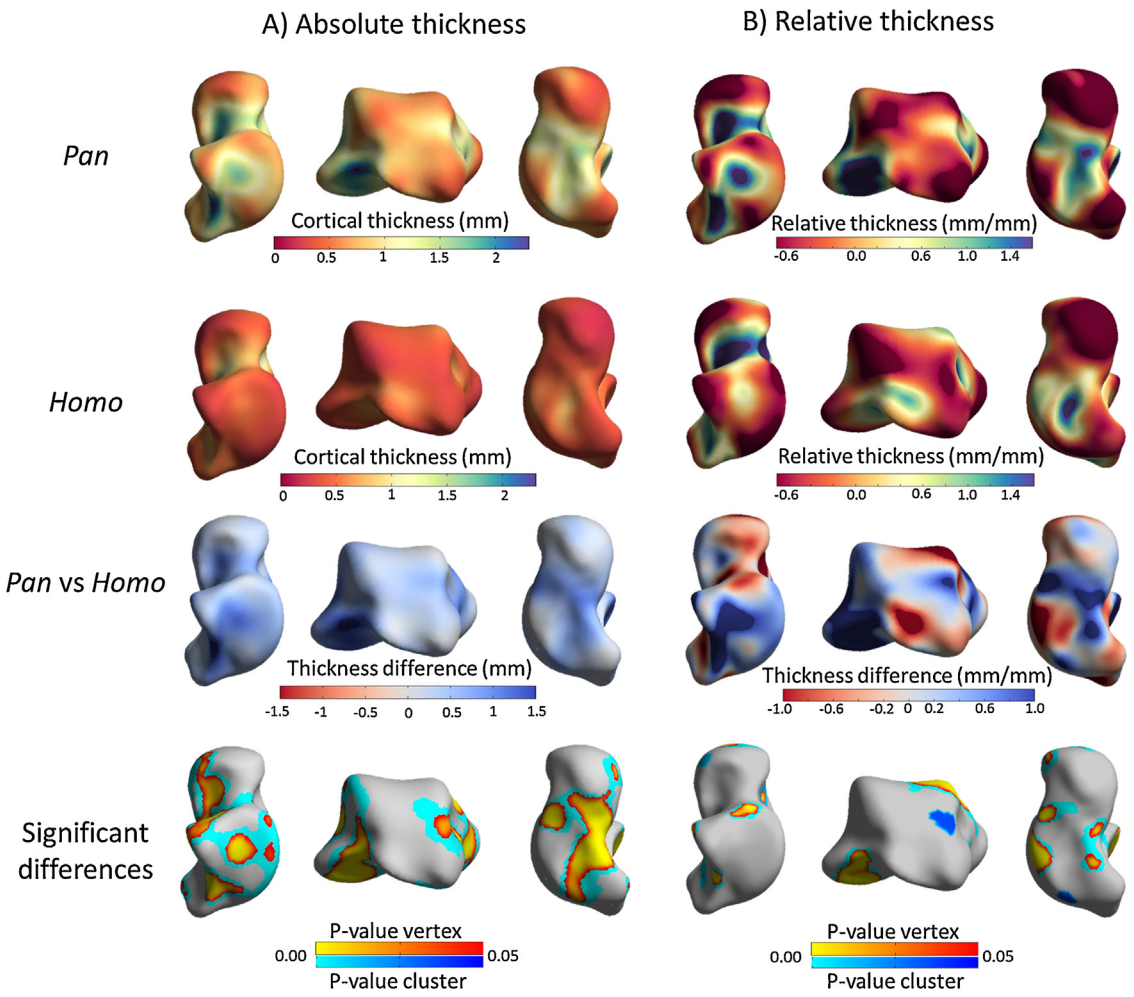

Fig. 6. Mean cortical thickness maps for the *Pan* and *Homo* talus showing results for both (A) absolute cortical thickness measurements and (B) relative cortical thickness comparisons. For relative thickness comparisons, the mean was subtracted from every thickness measurement then divided by the standard deviation for each individual before generating species averages and conducting statistical comparisons. From top to bottom, mean cortical thickness maps for *Pan*, mean cortical thickness maps for *Homo*, cortical thickness differences between *Pan* and *Homo* and statistical comparisons between the two species. Talus is shown in (from left to right) lateral, posterior and medial views.

Fig. 6. Distributions moyennes de l'épaisseur de l'os cortical pour le talus de *Pan* et *Homo* montrant les résultats pour (A) les mesures de l'épaisseur corticale absolue et (B) les comparaisons de l'épaisseur corticale relative. Pour ces dernières, la moyenne a été soustraite de chaque mesure d'épaisseur, puis divisée par l'écart-type, pour chaque individu, avant de générer des moyennes par espèce et de conduire des comparaisons statistiques. De haut en bas, distributions d'épaisseur corticale moyenne chez *Pan*, chez *Homo*, différences d'épaisseur corticale entre *Pan* et *Homo*, et comparaisons statistiques entre les deux espèces. De gauche à droite, le talus est montré en vues latérale, postérieure et médiale.

(e.g., a single slice) of cortical bone. However, this method does suffer from two shortcomings when comparing morphology that differs across samples. First, the automated method finds it challenging to register morphologically ambiguous regions, such as the relatively simple morphology of the shaft that lacks clearly identifiable features. Within palaeoanthropology, homology is often ensured by first selecting shared diagnostic features that can be easily and reproducibly identified, i.e., by using landmarks (e.g., Arias-Martorell et al., 2015; Knigge et al., 2015; Rein et al., 2015). This is not the case here, where correspondence is driven by proximity within a predefined search region. The method of registration applied here registers prominent morphological features, which would be appropriate for landmark placement, fairly effectively. However, in more featureless regions, such as the Mc3 shaft, the registration is not constrained by clear shape differences. Often in such transformations, there are ambiguous regions, such as the shaft, where multiple registrations could be argued to be valid resulting in a systematic misattribution of the mapped thickness. Even though we allowed for shape in the GLM, we were not able to allow for the dominant shape mode since it was highly correlated with group. It must therefore be kept in mind that the thickness differences identified may be the result of some systematic misregistration, especially since the lengths and widths of the Mc3 shafts across the hominoids in this sample are very different.

The second challenge with this method arises when morphology across the comparative sample differs

substantially. For example, *Homo* has a styloid process at the base of the Mc3 that is absent in non-human primates and most fossil hominins (Marzke and Marzke, 1987; Ward et al., 2013). However, the current method requires registering the entire comparative sample to a single surface, in this case an average mesh of the entire sample. In this study, the average mesh has a styloid process, and so the *Pan* and *Pongo* Mc3s are deformed during registration to a more *Homo*-like morphology. Thus, information taken from the base of the Mc3 is obscured and complicates interpretations of the potential differences in function, loading, and bony response. This has clear implications for testing hypotheses generated under the bone functional adaptation paradigm and will likely be an issue for other comparisons of skeletal elements that possess highly variable anatomical regions. Thus, with this method it would be necessary to mask or disregard such anatomical regions.

Indeed, the above issues are likely exaggerated within a (palaeo)anthropological context where small sample sizes are common and inter-species variation can be high. Although one might be able to collect a statistically significant number of high-resolution scans from *H. sapiens* or Neanderthals to be studied in this manner, most fossil hominin taxa are frequently only represented by one or two isolated and fragmentary specimens of any given anatomical element. As such, we should always be on the lookout for methods that allow us to gain as much data as possible from the available fossils (Zollikofer et al., 2001). Although any statistical analysis afforded by the present method will remain underpowered in regards to fossils, the ability to create interactive 3D visualizations provides a novel and informative way to compare morphology, and particularly morphological features that are attached to long-standing functional hypotheses (e.g., the functional significance of the Mc3 styloid process within humans, gracilization of the skeleton, or remodelling of bone at muscle attachment sites) and even help to generate new ones (see Hermann and Klein, 2015).

In light of this, a potential advantage of this 3D cortical mapping method is that the registration of individuals to a "mean mesh" produces information about shape differences across the sample. Principal component analysis produces a compact set of eigenvectors that capture the dominant modes of variation from the mean mesh. A statistical shape model of this nature can potentially be used to quantify and explore shape differences (Joshi et al., 2016; Schneider et al., 2015). In fact, the interactive visualization and deformation of the canonical model, by way of an associated statistical shape model file, is a feature that is currently available within wxRegSurf. This offers a quick and convenient way to visualise 3D shape/structure covariation, though whether the variation is biologically meaningful depends on the accuracy of the homologies.

The value of being able to visually evaluate variation in cortical thickness across the entire skeletal element is seen in comparison with previous cortical mapping techniques (Jashashvili et al., 2015; Puymerail et al., 2012a, 2012b; Ruff et al., 2015; Zollikofer et al., 2001) that rely on the cylindrical shape of long bones to digitally unroll the diaphysis and map thickness values onto a uniform grid (Bondioli et al., 2010). In contrast, thickness values in our 3D cortical mapping method are estimated on intact morphology using the width and height of the grey value curve within the user-specified measurement line. This type of measurement allows for an associated error range that is used to inform the weight of the smoothing algorithm and, subsequently, the mean values mapped to the canonical bone. Although some subtle variation is necessarily lost in this process, this allows for a reasonable estimation of cortical thickness in the individual and mean model, which can then be visualised qualitatively and statistically on the same mean model.

To conclude, the present method of cortical thickness measurement can be successfully applied to comparative samples, and builds upon previous techniques in palaeoanthropology by enabling cortical thickness measurement of more complex regions/elements, such as the epiphyses of the metacarpals and the talus. Through registration to a canonical model, statistical comparisons can be conducted between groups, which holds potential for applications to archaeological and fossil samples. However, in applying this method to comparative samples, it is important that the optimum morphology of the canonical mesh and the potential for misregistration are considered.

Acknowledgements

We thank Roberto Macchiarelli and Clément Zanolli for their invitation to contribute to this interesting special issue. We are grateful for the samples provided by the Berlin Museum für Naturkunde (Frieder Mayer), Max Planck Institute for Evolutionary Anthropology (Christophe Boesch), Museo Archeologico del Finale (Andrea De Pascale), Naturhistorisches Museum Wien (Maria Teschler-Nicola, Ronald Muehl), Senckenberg Museum (Virginie Volpato), University of Florence (Jacopo Moggi-Cecchi and Silvia Bortoluzzi), and University of Göttingen (Birgit Grosskopf). For scanning assistance we thank David Plotzki, Patrick Schönfeld, and Heiko Temming. For French translations we thank Adeline Le Cabec. This research was supported by the Max Planck Society (ZJT, NBS, MMS, TLK) and the European Research Council Starting Grant #336301 (TLK and MMS).

References

Arias-Martorell, J., Tallman, M., Potau, J.M., Bello-Hellegouarch, G., Pérez-Pérez, A., 2015. Shape analysis of the proximal humerus in orthograde and semi-orthograde primates: correlates of suspensory behavior. Am. J. Primatol. 77, 1–19.

Bondioli, L., Bayle, P., Dean, C., Mazurier, A., Puymerail, L., Ruff, C., Stock, J.T., Volpato, V., Zanolli, C., Macchiarelli, R., 2010. Technical note: morphometric maps of long bone shafts and dental roots for imaging topographic thickness variation. Am. J. Phys. Anthropol. 142, 328–334.

Carlson, K.J., 2005. Investigating the form-function interface in African apes: relationships between principal moments of area and positional behaviors in femoral and humeral diaphyses. Am. J. Phys. Anthropol. 127, 312–334.

Carlson, K.L., Judex, S., 2007. Increased non-linear locomotion alters diaphyseal bone shape. J. Exp. Bio. 210, 3117–3125.

Carlson, K.J., Doran-Sheehy, D.M., Hunt, K.D., Nishida, T., Yamanaka, A., Boesch, C., 2006. Locomotor behavior and long bone morphology in individual free-ranging chimpanzees. J. Hum. Evol. 50, 394–404.

Carlson, K.J., Jashashvili, T., Houghton, K., Westaway, M.C., Patel, B.A., 2013. Joint loads in marsupial ankles reflect habitual bipedalism

versus quadrupedalism. PLoS ONE 8, e58811, http://dx.doi.org/10.1371/journal.pone.0058811.
Carlson, K.J., Sumner, D.R., Morbeck, M.E., Nishida, T., Yamanaka, A., Boesch, C., 2008. Role of nonbehavioral factors in adjusting long bone diaphyseal structure in free-ranging *Pan troglodytes*. Int. J. Primatol. 29, 1401–1420.
Cashmore, L.A., Zakrzewski, S.R., 2013. Assessment of musculoskeletal stress marker development in the hand. Int. J. Osteoarchaeol. 23, 334–347.
Chirchir, H., Kivell, T.L., Ruff, C.B., Hublin, J.-J., Carlson, K.J., Zipfel, B., Richmond, B.G., 2015. Recent origins of low trabecular bone density in modern humans. Proc. Natl. Acad. Sci. U S A 112, 366–371.
Christen, P., Ito, K., Ellouz, R., Boutroy, S., Sornay-Rendu, E., Chapurlat, R.D., van Rietbergen, B., 2014. Bone remodelling in humans is load-driven but not lazy. Nat. Comm. 5, 4855, http://dx.doi.org/10.1038/ncomms5855.
Currey, J.D., 2003. The many adaptations of bone. J. Biomech. 36, 1487–1495.
Currey, J.D., 2010. Mechanical properties and adaptations of some less familiar bony tissues. J. Mech. Behav. Biomed. 3, 357–372.
Davies, T.G., Stock, J.T., 2014. The influence of relative body breadth on the diaphyseal morphology of the human lower limb. Am. J. Hum. Biol. 26, 822–835.
Demes, B., Qin, Y.-X., Stern Jr., J.T., Larson, S.G., Rubin, C.T., 2001. Patterns of strain in the macaque tibia during functional activity. Am. J. Phys. Anthropol. 116, 257–265.
Demes, B., Stern Jr., J.T., Hausman, M.R., Larson, S.G., McLeod, K.J., Rubin, C.T., 1998. Patterns of strain in the macaque ulna during functional activity. Am. J. Phys. Anthropol. 106, 87–100.
Friston, K.J., Holmes, A.P., Worsley, K.J., Poline, J.-P., Frith, C.D., Frackowiak, R.S.J., 1995. Statistical parametric maps in functional imaging: a general linear approach. Hum. Brain. Mapp. 2, 189–210.
Frost, H.M., 1987. Bone "mass" and the "mechanostat": a proposal. Anat. Rec. 219, 1–9.
Gee, A.H., Treece, G.M., 2014. Systematic misregistration and the statistical analysis of surface data. Med. Image Anal. 18, 385–393.
Gee, A.H., Treece, G.M., Tonkin, C.J., Black, D.M., Poole, K.E.S., 2015. Association between femur size and a focal defect of the superior femoral neck. Bone 81, 60–66.
Griffin, N.L., Richmond, B.G., 2005. Cross-sectional geometry of the human forefoot. Bone 37, 253–260.
Hermann, M., Klein, R., 2015. A visual analytics perspective on shape analysis: state of the art and future prospects. Comput. Graph. 53 (Part A), 63–71.
Jashashvili, T., Dowdeswell, M.R., Lebrun, R., Carlson, K.J., 2015. Cortical structure of hallucal metatarsals and locomotor adaptations in hominoids. PLoS ONE 10, e0117905, http://dx.doi.org/10.1371/journal.pone.0117905.
Joshi, A.A., Leahy, R.M., Badawi, R.D., Chaudhari, A.J., 2016. Registration-based morphometry for shape analysis of the bones of the human wrist. IEEE Trans. Med. Imaging 35, 416–426.
Knigge, R.P., Tocheri, M.W., Orr, C.M., McNulty, K.P., 2015. Three-dimensional geometric morphometric analysis of talar morphology in extant gorilla taxa from highland and lowland habitats. Anat. Rec. 298, 277–290.
Latimer, B., 1991. Locomotor adaptations in *Australopithecus afarensis*: the issue of arboreality. In: Senut, B., Coppens, Y. (Eds.), Origine(s) de la Bipédie chez les Hominidés. CNRS, Paris, pp. 169–176.
Lazenby, R.A., 1998. Second metacarpal midshaft geometry in an historic cemetery sample. Am. J. Phys. Anthropol. 106, 157–167.
Lieberman, D.E., Polk, J.D., Demes, B., 2004. Predicting long bone loading from cross-sectional geometry. Am. J. Phys. Anthropol. 123, 156–171.
Lillie, E.M., Urban, J.E., Weaver, A.A., Powers, A.K., Stitzel, J.D., 2015. Estimation of skull table thickness with clinical CT and validation with microCT. J. Anat. 226, 73–80.
Lovejoy, C.O., McCollum, M.A., Reno, P.L., Rosenman, B.A., 2003. Developmental biology and human evolution. Ann. Rev. Anthropol. 32, 85–109.
Marangoni, A., Belli, L.M., Caramelli, D., Jacopo, M.-C., Zavattaro, M., Manzi, G., 2011. The Tierra del Fuego, its ancient inhabitants, and the collections of human skeletal remains in the Museums of Anthropology of Florence and Rome. Museological significance, past researches, perspectives. Museol. Sci. 5, 88–96.
Marchi, D., 2005. The cross-sectional geometry of the hand and foot bones of the Hominoidea and its relationship to locomotor behaviour. J. Hum. Evol. 49, 743–761.
Marzke, M.W., Marzke, R.F., 1987. The third metacarpal styloid process in humans: origin and functions. Am. J. Phys. Anthropol. 73, 415–431.
Mazurier, A., Nakatsukasa, M., Macchiarelli, R., 2010. The inner structural variation of the primate tibial plateau characterized by high-resolution microtomography. Implications for the reconstruction of fossil locomotor behaviours. C. R. Palevol 9, 349–359.
Paoli, G., Tarli, S.M.B., Klir, P., Strouhal, E., Tofanelli, S., Valli, M.T.D., Pavelcova, B., 1993. Paleoserology of the Christian population at Sayala (Lower Nubia) – an evaluation of the reliability of the results. Am. J. Phys. Anthropol. 92, 263–272.
Patel, B.A., Carlson, K.J., 2007. Bone density spatial patterns in the distal radius reflect habitual hand postures adopted by quadrupedal primates. J. Hum. Evol. 52, 130–141.
Pearson, O.M., Lieberman, D.E., 2004. The aging of Wolff's "law": ontogeny and responses to mechanical loading in cortical bone. Yearb. Phys. Anthropol. 47, 63–99.
Poole, K.E.S., Treece, G.M., Mayhew, P.M., Vaculík, J., Dungl, P., Horák, M., Štěpán, J.J., Gee, A.H., 2012. Cortical thickness mapping to identify focal osteoporosis in patients with hip fracture. PLoS ONE 7, e38466, http://dx.doi.org/10.1371/journal.pone.0038466.
Poole, K.E.S., Treece, G.M., Ridgway, G.R., Mayhew, P.M., Borggrefe, J., Gee, A.H., 2011. Targeted regeneration of bone in the osteoporotic human femur. PLoS ONE 6, e16190, http://dx.doi.org/10.1371/journal.pone.0016190.
Puymerail, L., 2013. The functionally-related signatures characterizing the endostructural organisation of the femoral shaft in modern humans and chimpanzee. C. R. Palevol 12, 223–231.
Puymerail, L., Ruff, C.B., Bondioli, L., Widianto, H., Trinkaus, E., Macchiarelli, R., 2012a. Structural analysis of the Kresna 11 *Homo erectus* femoral shaft (Sangiran, Java). J. Hum. Evol. 63, 741–749.
Puymerail, L., Volpato, V., Debénath, A., Mazurier, A., Tournepiche, J.-F., Macchiarelli, R., 2012b. A Neanderthal partial femoral diaphysis from the "grotte de la Tour", La Chaise-de-Vouthon (Charente, France): outer morphology and endostructural organization. C. R. Palevol 11, 581–593.
Rabey, K.N., Green, D.J., Taylor, A.B., Begun, D.R., Richmond, B.G., McFarlin, S.C., 2015. Locomotor activity influences muscle architecture and bone growth but not muscle attachment site morphology. J. Hum. Evol. 78, 91–102.
Rein, T.R., Harvati, K., Harrison, T., 2015. Inferring the use of forelimb suspensory locomotion by extinct primate species via shape exploration of the ulna. J. Hum. Evol. 78, 70–79.
Robling, A.G., Hinant, F.M., Burr, D.B., Turner, C.H., 2002. Improved bone structure and strength after long-term mechanical loading is greatest if loading is separated into short bouts. J. Bone Miner. Res. 17, 1545–1554.
Ruff, C.B., 2002. Long bone articular and diaphyseal structure in Old World monkeys and apes. I: locomotor effects. Am. J. Phys. Anthropol. 11, 305–342.
Ruff, C.B., 2008. Femoral/humeral strength in early African *Homo erectus*. J. Hum. Evol. 54, 383–390.
Ruff, C.B., Burgess, M.L., Bromage, T.G., Mudakikwa, A., McFarlin, S.C., 2013. Ontogenetic changes in limb bone structural proportions in mountain gorillas (*Gorilla beringei beringei*). J. Hum. Evol. 65, 693–703.
Ruff, C.B., Holt, B., Trinkhaus, E., 2006. Who's afraid of the big bad Wolff?: "Wolff's law" and bone functional adaptation. Am. J. Phys. Anthropol. 129, 484–498.
Ruff, C.B., Puymerail, L., Macchiarelli, R., Sipla, J., Ciochon, R.L., 2015. Structure and composition of the Trinil femora: functional and taxonomic implications. J. Hum. Evol. 80, 147–158.
Ryan, T.M., Shaw, C.N., 2015. Gracility of the modern *Homo sapiens* skeleton is the result of decreased biomechanical loading. Proc. Natl. Acad. Sci. U S A 112, 372–377.
Sarringhaus, L.A., Stock, J.T., Marchant, L.F., McGrew, W.C., 2005. Bilateral asymmetry in the limb bones of the chimpanzee (*Pan troglodytes*). Am. J. Phys. Anthropol. 128, 840–845.
Schneider, M.T.Y., Zhang, J., Crisco, J.J., Weiss, A.P.C., Ladd, A.L., Nielsen, P., Besier, T., 2015. Men and women have similarly shaped carpometacarpal joint bones. J. Biomech. 12, 3420–3426.
Shaw, C.N., Stock, J.T., 2013. Extreme mobility in the Late Pleistocene? Comparing limb biomechanics among fossil *Homo*, varsity athletes and Holocene foragers. J. Hum. Evol. 64, 242–249.
Smith, R.J., Jungers, W.L., 1997. Body mass in comparative primatology. J. Hum. Evol. 32, 523–559.
Sparacello, V., Pettitt, P.B., Roberts, C., 2015. Funerary dynamics of an Epipalaeolithic cemetery: a new database on Arene Candide skeletal remains. Proc. Europ. Soc. Study Hum. Evol. 4, 209 (abstract).
Stern Jr., J.T., 2000. Climbing to the top: a personal memoir of *Australopithecus afarensis*. Evol. Anthropol. 9, 113–133.

Strouhal, E., Jungwirth, J., 1979. Paleogenetics of the Late Roman-Early Byzantine cemeteries at Sayala, Egyptian Nubia. J. Hum. Evol. 8, 699–703.

Treece, G.M., Gee, A.H., Mayhew, P.M., Poole, K.E.S., 2010. High-resolution cortical bone thickness measurement from clinical CT data. Med. Image Anal. 14, 276–290.

Treece, G.M., Poole, K.E.S., Gee, A.H., 2012. Imaging the femoral cortex: thickness, density and mass from clinical CT. Med. Image Anal. 16, 952–965.

Wallace, I.J., Gupta, S., Sankaran, J., Demes, B., Judex, S., 2015a. Bone shaft bending strength index is unaffected by exercise and unloading in mice. J. Anat. 226, 224–228.

Wallace, I.J., Judex, S., Demes, B., 2015b. Effects of load-bearing exercise on skeletal structure and mechanics differ between outbred populations of mice. Bone 72, 1–8.

Ward, C.V., 2002. Interpreting the posture and locomotion of *Australopithecus afarensis*: where do we stand? Yearb. Phys. Anthropol. 45, 185–215.

Ward, C.V., Tocheri, M.W., Plavcan, J.M., Brown, F.H., Manthi, F.K., 2013. Early Pleistocene third metacarpal from Kenya and the evolution of modern human-like hand morphology. Proc. Natl. Acad. Sci. U S A 111, 121–124.

Williams-Hatala, E.M., Hatala, K.G., Hiles, S., Rabey, K.N., 2016. Morphology of muscle attachment sites in the modern human hand does not reflect muscle architecture. Sc. Rep. 6, 28353, http://dx.doi.org/10.1038/srep28353.

Worsley, K.J., Taylor, J.E., Carbonell, F., Chung, M.K., Duerden, E., Bernhardt, B., Lyttelton, O., Boucher, M., Evans, A.C., 2009. SurfStat: A Matlab Toolbox for the Statistical Analysis of Univariate and Multivariate Surface and Volumetric Data Using Linear Mixed Effects Models and Random Field Theory. NeuroImage Organization for Human Brain Mapping, San Francisco, CA, USA, pp. S102.

Zollikofer, C.P., Ponce de León, M., De Bonis, L., Koufos, G., Andrews, P., 2001. Computer-assisted morphometry of hominoid fossils: The role of morphometric maps. In: de Bonis, L., Koufos, G.D., Andrews, P. (Eds.), Phylogeny of the Neogene Hominoid Primates of Eurasia. Cambridge University Press, Cambridge, UK, pp. 50–59.